

This document contains a post-print version of the paper

## Modelling and Experimental Model Validation for a Pusher-type Reheating Furnace

authored by D. Wild, T. Meurer, and A. Kugi

and published in *Mathematical and Computer Modelling of Dynamical Systems*.

---

The content of this post-print version is identical to the published paper but without the publisher's final layout or copy editing. Please, scroll down for the article.

---

### Cite this article as:

D. Wild, T. Meurer, and A. Kugi, "Modelling and experimental model validation for a pusher-type reheating furnace", *Mathematical and Computer Modelling of Dynamical Systems*, vol. 15, no. 3, pp. 209–232, 2009. DOI: [10.1080/13873950902927683](https://doi.org/10.1080/13873950902927683)

---

### BibTex entry:

```
@article{Wild09,  
  author = {Wild, D. and Meurer, T. and Kugi, A.},  
  title = {Modelling and Experimental Model Validation for a Pusher-type Reheating Furnace},  
  journal = {Mathematical and Computer Modelling of Dynamical Systems},  
  year = {2009},  
  volume = {15},  
  number = {3},  
  pages = {209--232},  
  doi = {10.1080/13873950902927683},  
  url = {http://www.tandfonline.com/doi/abs/10.1080/13873950902927683}  
}
```

---

### Link to original paper:

<http://dx.doi.org/10.1080/13873950902927683>  
<http://www.tandfonline.com/doi/abs/10.1080/13873950902927683>

---

### Read more ACIN papers or get this document:

<http://www.acin.tuwien.ac.at/literature>

---

### Contact:

Automation and Control Institute (ACIN)  
Vienna University of Technology  
Gusshausstrasse 27-29/E376  
1040 Vienna, Austria

Internet: [www.acin.tuwien.ac.at](http://www.acin.tuwien.ac.at)  
E-mail: [office@acin.tuwien.ac.at](mailto:office@acin.tuwien.ac.at)  
Phone: +43 1 58801 37601  
Fax: +43 1 58801 37699

---

### Copyright notice:

This is an authors' accepted manuscript of the article D. Wild, T. Meurer, and A. Kugi, "Modelling and experimental model validation for a pusher-type reheating furnace", *Mathematical and Computer Modelling of Dynamical Systems*, vol. 15, no. 3, pp. 209–232, 2009. DOI: [10.1080/13873950902927683](https://doi.org/10.1080/13873950902927683) published in *Mathematical and Computer Modelling of Dynamical Systems*, copyright © Taylor & Francis Group, LLC, available online at: <http://dx.doi.org/10.1080/13873950902927683>

## Modelling and Experimental Model Validation for a Pusher-type Reheating Furnace

D. Wild, T. Meurer, A. Kugi  
Automation and Control Institute,  
Complex Dynamical Systems Group,  
Vienna University of Technology, Vienna, Austria,  
{wild, meurer, kugi}@acin.tuwien.ac.at

The slab reheating process turns out to play a key role in order to deal with the steadily increasing demands on the quality of hot rolled steel plates. Improvements both in the throughput of the furnace as well as the accurate realization of reheating paths for the slabs require to incorporate modern model-based control design techniques into the furnace automation. For this, suitable mathematical models with manageable dimension and complexity have to be determined for the furnace and slab dynamics. In this contribution, first principles are applied for the derivation of a physics-based model of the reheating process in a so-called pusher-type reheating furnace. Thereby, a discontinuous mode of furnace operation is considered, which is characterized by a varying number of slabs with variable geometry being discontinuously moved through the furnace. This in particular results in a hybrid structure of the mathematical model. The accuracy of the mathematical model is validated by a comparison with experimental data obtained from a measurement campaign with a test slab performed at an industrial pusher-type reheating furnace.

*Keywords:* Pusher-type furnace, slab reheating process, physics-based modelling, combustion modelling, singular perturbation, experimental validation

### 1. Introduction

Reheating of slabs from the ambient temperature to their rolling temperature of approximately 1150°C is an important step in the heavy plate production in order to prepare the slabs for the subsequent rolling process. For this, the slabs are normally heated in gas- or oil-fired pusher-type reheating furnaces.

In order to illustrate this, a schematic setup of the furnace, which is considered in the following, is shown in Figure 1. Depending on the location of the burners, the local temperature range, and the dwell of the slabs, the furnace can be structurally divided into the convective zone without burners, the pre-heating zone, the heating zone as well as the pre-soaking and the soaking zone. In the convective zone an initial heating of the cold slabs entering the furnace occurs due to the heat radiation and the convective flow of hot exhaust gas which is directed towards the funnel. In the two heating zones the slabs are heated up to their pre-planned rolling temperature in order to achieve the desired metallurgical transitions. The homogenisation of the slabs by diffusive processes inside the material finally occurs in the two soaking zones. Note that every zone except the convective zone is equipped with burners whose fuel and combustion air flows can be adjusted autonomously for each zone.

In the typical operation mode cold slabs are pushed into the furnace in up to three parallel rows at the position  $z = 0$  while the readily heated slabs are pulled out of the furnace on the opposite side at  $z = L_z$ . Note that new slabs can only enter the furnace whenever heated slabs are pulled out of the furnace. The majority of pusher-type furnaces is continuously fed with slabs of the same geometry such that the furnace is operated in a quasi-steady state with rather constant working conditions. However, depending on the integration of the pusher-type furnace within the overall production process, configurations arise where the furnace is fed discontinuously with slabs of varying geometry and differing desired heating and homogenisation paths. Due to the coupling of the time-continuous heat exchange and flow processes with the discrete switching of the slab movement along the  $z$ -direction, the thus operated pusher-type furnace

---

Gusshausstrasse 27-29 / E376, A-1040 Vienna, Austria, Phone: +43 (0)1 58801-77628, Fax: +43 (0)1 58801-37699

*Mathematical and Computer Modelling of Dynamical Systems*  
ISSN: 1387-3954 print/ISSN 1744-5051 online © 2004 Taylor & Francis  
<http://www.tandf.co.uk/journals>  
DOI: 10.1080/13873950xxxxxxxxxxxx

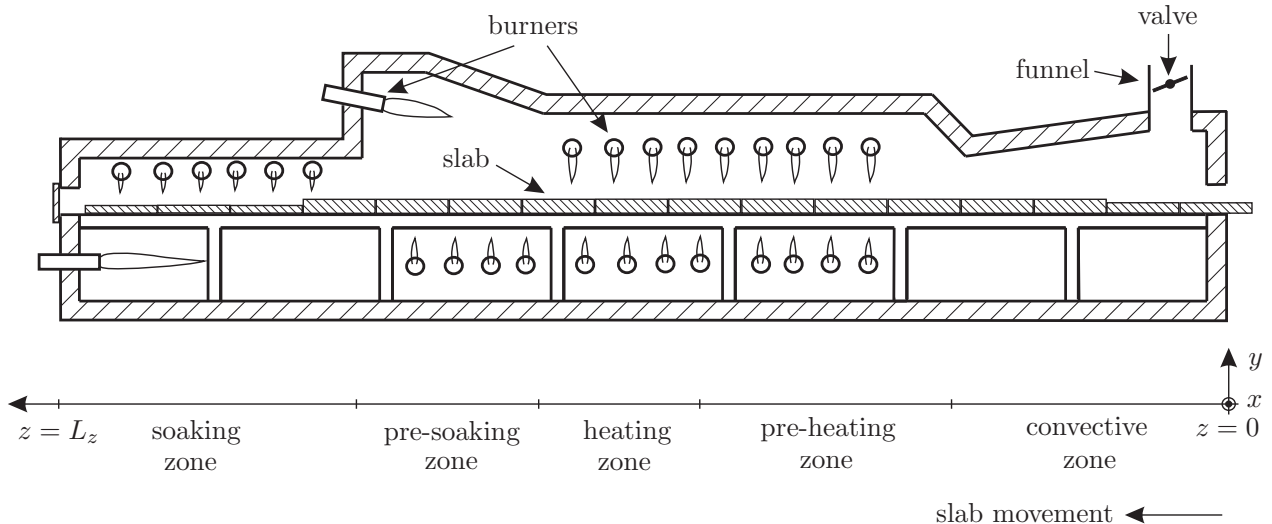


Figure 1. Schematic illustration of a typical pusher-type reheating furnace heated with gas and/or oil burners.

can be classified as a hybrid system.

This operation mode in particular requires to include state-of-the-art automation facilities in order to cope with the steadily increasing demands on product quality and the increasing production rates in hot rolling mills. For this, both advanced optimization strategies to determine the suitable entering sequence of the slabs in view of their individual heating and homogenisation paths and modern model-based control techniques to realize the heating strategy have to be incorporated. Thereby, the major difficulty is the fact that it is desired to control the individual slab temperatures without the possibility to measure the slab temperatures inside the furnace. Hence, an appropriate mathematical model has to be derived in order to numerically reconstruct the slab temperatures during the reheating process. Thereby, on the one hand the highly complex furnace dynamics including the combustion of fuel, the gas mass flows within the non-trivial geometry of the furnace and the energy exchange between the slabs, the gas and the walls has to be captured by a suitable mathematical model. On the other hand, a manageable complexity of the mathematical model has to be retained in view of control design and its real-time implementation.

For computational modelling, system analysis, and simulation, the application of methods originating from computational fluid dynamics (CFD) often allows to obtain an accurate spatial and temporal resolution of the mass flow and heat transfer mechanisms inside the furnace. However, these advantages of CFD-based approaches are overwhelmed by the large number of system variables reaching up to several million quantities depending on the level of detail. Hence these tools are commonly used for designing new furnaces and to perform off-line studies of the gas and/or combustion dynamics [1, 2]. A reduction of the calculating time compared to conventional CFD techniques is achieved by combining the CFD simulation with the classical zone method [3]. Although providing promising results in view of resolving the gas dynamics and the heat transfer mechanisms, this approach still lacks to provide analytical mathematical models of medium complexity and dimension, which are the basis for model-based control design.

On the other hand, in many industrial applications a pragmatic modelling approach is considered, which traces back to [4]. Therein, a sufficiently large number of local furnace temperature measurements obtained from suitably distributed thermocouples serve as inputs for a slab-heating model, see, e.g., [5, 6]. This allows to evaluate the respective slab temperature profiles in real-time. In view of control design as well as process optimization the main drawback of this approach arises from the missing relation between the measured furnace temperatures and their realization by the physical inputs, namely fuel and combustion air.

As a promising alternative avoiding the high number of system variables while preserving the physical relation between the system state and input quantities, the so-called zone method as proposed in [7], is extensively studied in [8, 9]. Thereby, the furnace is subdivided into gas volumes, wall and slab elements whose radiative heat exchange is calculated utilizing coupling factors. Furthermore, this approach assumes a continuous furnace operation mode and steady state conditions for the wall and gas temperature. The

available results on furnace modelling utilizing the zone method are based on the assumption of a continuous furnace operation, i.e. uniform slab geometries, target temperatures, and slab movements. However, this is no longer satisfied in the furnace under consideration.

Therefore, in the following a physics-based modelling approach is considered for the discontinuous operation mode of the reheating furnace depicted in Figure 1. For this, according to the zone method, in Section 2 the furnace is discretized along the  $z$ -direction into control volumes. In each control volume, mass and energy balances are applied for modelling the dynamics of the exhaust gas composition as well as the respective gas temperature. In addition, the temperature evolution in the surrounding wall elements and the slabs is incorporated in the system description. Since thermal radiation represents the major mode of energy exchange inside the furnace, the so-called net-radiation method is used in Section 3 to determine the heat flows coupling the individual sub-models of the gas composition, the gas temperature, the wall temperature, and the slab temperature inside the furnace. This is followed by the assembling of the sub-models into a single model describing the overall reheating process in the furnace. Furthermore, a brief discussion on the computational implementation of this model is given in Section 4. The accuracy of the determined model is validated in Section 5 by comparing numerical results and measurement data obtained from a measurement campaign at the AG der Dillinger Hüttenwerke, Dillingen (Germany). Some final remarks conclude the paper.

#### Nomenclature of some important quantities

$A_{s_j}^i$	area of the $j$ -th slab surface inside the $i$ -th control volume
$A_{s_j}$	surface area of the $j$ -th slab
$A_{w_i}$	surface area of the $i$ -th wall element
$\dot{Q}_{g_i, s_j}$	heat flow between the $i$ -th gas space and the $j$ -th slab surface
$\dot{Q}_{g_i, w_k}$	heat flow between the $i$ -th gas space and the $k$ -th wall surface
$\dot{Q}_{w_i, s_j}$	heat flow between the $i$ -th wall and the $j$ -th slab surface
$g_i$	index denoting the $i$ -th control volume, $i = 1, \dots, 2N_v$
$\dot{m}_{g_i}^a$	combustion air mass flow into the $i$ -th control volume
$\dot{m}_{g_i}^f$	fuel mass flow into the $i$ -th control volume
$\dot{m}_{g_i}^{in}$	mass flow into the $i$ -th control volume, i.e. out of the $(i+1)$ -th into the $i$ -th control volume
$\dot{m}_{g_i}^{out}$	mass flow out of the $i$ -th control volume, i.e. out of the $i$ -th into the $(i-1)$ -th control volume
$N_{slab}$	number of slabs charged into the furnace
$N_v$	number of discretized control volumes of a furnace section
$s_j$	index denoting the $j$ -th slab, $j = 1, \dots, N_{slab}$
$\mathbf{T}_g$	vector of the gas temperatures $T_{g_i}$ for $i = 1, \dots, 2N_v$
$\mathbf{T}_s$	vector combining all slab temperature vectors $\mathbf{T}_{s_j}$ of all slabs for $j = 1, \dots, N_{slab}$
$\mathbf{T}_w$	vector of the wall surface temperatures $T_{w_i}$ for $i = 1, \dots, 2N_v$
$\mathbf{u}_g$	vector combining all input vectors $\mathbf{u}_{g_i}$ of all control volumes for $i = 1, \dots, 2N_v$
$\mathbf{w}_g$	vector combining all vectors $\mathbf{w}_{g_i}$ of all control volumes for $i = 1, \dots, 2N_v$
$T_{g_i}$	gas temperature in the $i$ -th control volume
$T_{s_j}$	temperature distribution along the height of the $j$ -th slab, i.e. $T_{s_j}(t, y)$
$\mathbf{T}_{s_j}$	vector of the spatially discretized temperatures $T_{s_j}$ of the $j$ -th slab
$T_{w_i}$	wall surface temperature of the $i$ -th wall element
$\mathbf{u}_{g_i}$	input vector of the $i$ -th control volume
$\mathbf{w}_{g_i}$	vector of mass fractions of all species inside the $i$ -th control volume
$w_i$	index denoting the wall surrounding the $i$ -th control volume, $i = 1, \dots, 2N_v$
$w_{g_i}^\nu$	mass fraction of the $\nu$ -th species in the $i$ -th control volume

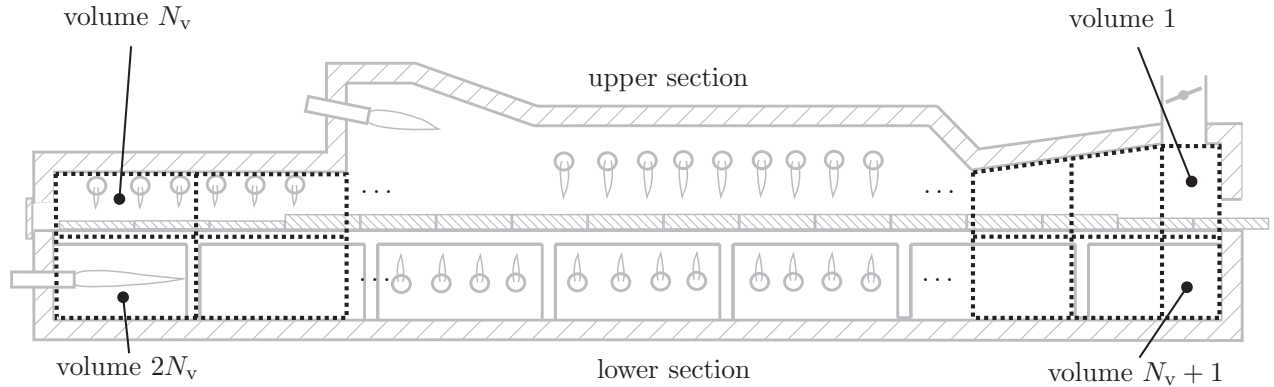


Figure 2. Schematic illustration of the furnace discretization into control volumes for the upper (volumes 1 to  $N_v$ ) and the lower furnace section (volumes  $N_v + 1$  to  $2N_v$ ).

## 2. Mathematical modelling

In this section, a physics-based mathematical model is presented for the pusher-type reheating furnace shown in Figure 1. It is thereby desired that the derived model accurately reflects the fundamental dynamics of the reheating process. Secondary and from a modelling and validation point of view only hardly accessible effects such as the detailed fluid flow within the furnace or the influence of the flame geometry are neglected in order to retain a model of manageable dimension and complexity.

For modelling purposes, the furnace is split up into an upper and a lower section as shown in Figure 2. According to the zone method [7, 10], each section is divided into  $N_v$  control volumes with respect to the  $z$ -direction in order to accurately approximate the furnace shape and to ensure that (almost) every control volume contains a thermocouple. Note that the latter requirement is in particular important for the subsequent experimental validation.

Furthermore, it is assumed that temperature deviations occur only along the  $z$ -coordinate, i.e. over the length of the furnace. This simplification is motivated by the fact that all burners within a furnace zone are actuated by a common valve for fuel and combustion air, such that it is not directly possible to influence the temperature distribution along the width and height of the upper and lower furnace section. In the following, the governing equations for the exhaust gas composition as well as the gas temperature, the wall temperature, and the slab temperature distribution are exemplarily derived for the  $i$ -th control volume and the  $j$ -th slab by applying first principles. The overall system model can then be easily assembled from these subsystems.

### 2.1. Gas and combustion dynamics

For the modelling of the exhaust gas dynamics, at first the components  $G$  of the furnace atmosphere are identified and divided into the sets  $G_o$ ,  $G_a$ , and  $G_e$  denoting the oxidizable components, the combustion air components, and the combustion products, i.e. the exhaust gas generated from the combustion of  $G_o$  with  $G_a$ , respectively. In particular, the oxidizable components can be identified as hydrogen ( $H_2$ ), carbon monoxide ( $CO$ ), and hydrocarbon gases like methane ( $CH_4$ ), ethane ( $C_2H_6$ ), etc., such that  $G_o$  is given in the form  $G_o = \{H_2, CO, CH_4, C_2H_6, \dots\}$ . The combustion air is assumed to be a mixture of nitrogen ( $N_2$ ) and oxygen ( $O_2$ ), i.e.  $G_a = \{N_2, O_2\}$ . Hence, the resulting group of exhaust gases consists mainly of the combustion products vapor ( $H_2O$ ) and carbon dioxide ( $CO_2$ ), i.e.  $G_e = \{H_2O, CO_2\}$ . In order to increase the level of detail also incomplete combustion and dissociation products can be included in  $G_e$ . In the following, the composition of the mass  $m_{g_i}$  of gas stored in the  $i$ -th control volume is expressed in terms of mass fractions  $w_{g_i}^\nu$  such that the mass of an individual component  $\nu \in G = G_o \cup G_a \cup G_e$  inside the volume is given by  $m_{g_i}^\nu = m_{g_i} w_{g_i}^\nu$  while  $\sum_{\nu \in G} w_{g_i}^\nu = 1$ .

As illustrated in Figure 1, the mass flow in each control volume is dominated by the flow directed towards the funnel, i.e. in the sequel it is assumed that all mass flows are oriented in negative  $z$ -direction.

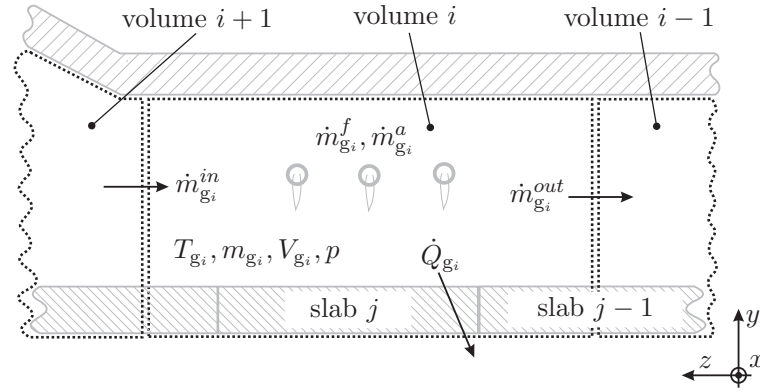


Figure 3. Schematic diagram of the  $i$ -th control volume.

Furthermore, we assume an isobaric furnace process at constant pressure  $p$ , which is ensured in the real plant by an appropriately controlled valve inside the funnel. Considering the  $i$ -th control volume as shown in Figure 3, the mass flows entering and leaving the control volume are denoted as  $\dot{m}_{g_i}^{in}$  and  $\dot{m}_{g_i}^{out}$ , respectively. The quantities  $\dot{m}_{g_i}^f$  and  $\dot{m}_{g_i}^a$  describe the fuel and air mass flow into the volume due to the attached burners. The respective compositions are similarly expressed by the mass fractions  $w_{g_i}^{in,\nu}$ ,  $w_{g_i}^{out,\nu}$ ,  $w_{g_i}^{f,\nu}$ , and  $w_{g_i}^{a,\nu}$ . In order to simplify the notation, in the subsequent mass balances the sum of the fuel and air mass flows are abbreviated by  $\dot{m}_{g_i}^b = \dot{m}_{g_i}^f + \dot{m}_{g_i}^a$  while the respective mass fraction follows as  $w_{g_i}^{b,\nu} = (\dot{m}_{g_i}^f w_{g_i}^{f,\nu} + \dot{m}_{g_i}^a w_{g_i}^{a,\nu}) / \dot{m}_{g_i}^b$ . According to Figure 3 mass conservation of the stored mass  $m_{g_i}$  inside the control volume  $V_{g_i}$  yields

$$\frac{dm_{g_i}}{dt} = \dot{m}_{g_i}^{in} + \dot{m}_{g_i}^b - \dot{m}_{g_i}^{out} \quad (1)$$

while mass balancing for the respective components  $\nu \in G$  results in

$$\frac{dm_{g_i}^\nu}{dt} = \dot{m}_{g_i}^{in} w_{g_i}^{in,\nu} + \dot{m}_{g_i}^b w_{g_i}^{b,\nu} - \dot{m}_{g_i}^{out} w_{g_i}^{out,\nu} + V_{g_i} M^\nu \dot{r}_{g_i}^\nu. \quad (2)$$

Here, the term  $M^\nu$  denotes the molar weight of the component  $\nu$  while  $\dot{r}_{g_i}^\nu$  represents the mass generation rate of the component  $\nu$  resulting from the chemical reactions of the combustion process. Hence, a positive generation rate  $\dot{r}_{g_i}^\nu > 0$  indicates the production of the species  $\nu$  while a negative generation rate  $\dot{r}_{g_i}^\nu < 0$  indicates the degradation of  $\nu$  [11]. Note that the generation rate  $\dot{r}_{g_i}^\nu$  in general depends on the temperature of the reactants and their mass fractions  $w_{g_i}^\nu$  inside the control volume and will be discussed below. Substitution of (1) into (2) and assuming ideal mixing conditions inside the gas volume, i.e.  $w_{g_i}^{out,\nu} = w_{g_i}^\nu$  for all  $\nu \in G$ , a set of ordinary differential equations (ODEs)

$$m_{g_i} \frac{dw_{g_i}^\nu}{dt} = \dot{m}_{g_i}^{in} (w_{g_i}^{in,\nu} - w_{g_i}^\nu) + \dot{m}_{g_i}^b (w_{g_i}^{b,\nu} - w_{g_i}^\nu) + V_{g_i} M^\nu \dot{r}_{g_i}^\nu, \quad \nu \in G \quad (3)$$

for the mass fractions is obtained in terms of the incoming mass flows, their mass fractions, and the reaction rate. Recall that the considered furnace is operated at a constant pressure  $p$ . Hence, by assuming ideal-gas behavior, the stored mass  $m_{g_i}$  in the  $i$ -th control volume with volume  $V_{g_i}$  can be easily determined from the ideal gas law as a function of the gas temperature  $T_{g_i}$  and the mass fractions  $w_{g_i}^\nu$ ,  $\nu \in G$ , i.e.

$$m_{g_i} = \frac{pV_{g_i}}{RT_{g_i} \sum_{\nu \in G} \frac{w_{g_i}^\nu}{M^\nu}} \quad (4)$$

with  $R$  the universal gas constant [12]. Hence, for given  $\dot{m}_{g_i}^{in}$  and  $\dot{m}_{g_i}^b$  differentiation of (4) with respect

to time  $t$  in view of (3) allows to compute the mass flow  $\dot{m}_{g_i}^{out}$  leaving the control volume. However, this requires the knowledge of the time evolution of the gas temperature  $T_{g_i}$ .

For this, the energy balance for the control volume is set up by considering the change of the stored enthalpy  $H_{g_i}$ , i.e.

$$\frac{dH_{g_i}}{dt} = -\dot{Q}_{g_i} + \dot{H}_{g_i}^b + \dot{H}_{g_i}^{in} - \dot{H}_{g_i}^{out}, \quad (5)$$

where  $\dot{Q}_{g_i}$  summarizes the energy exchange between the gas volume and the slabs as well as the walls. A detailed calculation of  $\dot{Q}_{g_i}$  is given in Section 3. The enthalpy flow  $\dot{H}_{g_i}^b$  from the burners consists of the enthalpies associated with the fuel mass flow  $\dot{m}_{g_i}^f$  at temperature  $T_{g_i}^f$  and with the mass flow of the pre-heated air  $\dot{m}_{g_i}^a$  at temperature  $T_{g_i}^a$ . This yields

$$\dot{H}_{g_i}^b = \dot{m}_{g_i}^f \sum_{\nu \in G_f} w_{g_i}^{f,\nu} h^\nu(T_{g_i}^f) + \dot{m}_{g_i}^a \sum_{\nu \in G_a} w_{g_i}^{a,\nu} h^\nu(T_{g_i}^a), \quad (6)$$

where  $h^\nu(T)$  denotes the absolute specific enthalpy<sup>1</sup> of the species  $\nu$  at temperature  $T$  and  $G_f \subset G$  summarizes the components of the fuel. Note that typically the furnaces used in hot rolling mills are fired with not necessarily constant mixtures of coke oven gas, natural gas, and blast furnace gas. Hence, the fuel is a mixture of oxidizable and non-combustible components. Since  $G_f \subset G$ , the subsequent notation is simplified by extending  $w_{g_i}^{f,\nu}$  and  $w_{g_i}^{a,\nu}$  to  $G$  with the choice  $w_{g_i}^{f,\nu} = 0$  and  $w_{g_i}^{a,\nu} = 0$  if  $\nu \in G$  but  $\nu \notin G_f$  or  $\nu \notin G_a$ , respectively.

Besides the energy input from the burners, the exhaust gas  $\dot{m}_{g_i}^{in}$  from the previous control volume enters the considered control volume at the temperature  $T_{g_i}^{in}$ . Equivalently, energy is transferred to the next control volume by the mass flow  $\dot{m}_{g_i}^{out}$  at the temperature  $T_{g_i}^{out}$  such that

$$\dot{H}_{g_i}^{in} = \dot{m}_{g_i}^{in} \sum_{\nu \in G} w_{g_i}^{in,\nu} h^\nu(T_{g_i}^{in}), \quad \dot{H}_{g_i}^{out} = \dot{m}_{g_i}^{out} \sum_{\nu \in G} w_{g_i}^{out,\nu} h^\nu(T_{g_i}^{out}). \quad (7)$$

Recall that the stored mass-specific enthalpy is given as  $H_{g_i} = m_{g_i} h_{g_i}$  with the mass specific enthalpy  $h_{g_i} = \sum_{\nu \in G} h^\nu(T_{g_i}) w_{g_i}^\nu$ . Hence, by considering the total differential of the mass-specific enthalpy of the mixture inside the control volume under isobaric conditions [11], i.e.  $dh_{g_i} = c_{p,g_i} dT_{g_i} + \sum_{\nu \in G} h^\nu dw_{g_i}^\nu$  with the specific heat capacity for ideal mixtures of the gas components  $c_{p,g_i} = \sum_{\nu \in G} w_{g_i}^\nu c_{p,g_i}^\nu$ ,  $c_{p,g_i}^\nu = \partial h^\nu / \partial T_{g_i} |_{w_{g_i}^\nu}$ , it follows in view of (5) with (2), (6), (7) that

$$m_{g_i} c_{p,g_i} \frac{dT_{g_i}}{dt} = -\dot{Q}_{g_i} - V_{g_i} \sum_{\nu \in G} M^\nu \dot{r}_{g_i}^\nu h^\nu(T_{g_i}) + \dot{m}_{g_i}^{in} \sum_{\nu \in G} w_{g_i}^{in,\nu} [h^\nu(T_{g_i}^{in}) - h^\nu(T_{g_i})] + \dot{m}_{g_i}^f \sum_{\nu \in G} w_{g_i}^{f,\nu} [h^\nu(T_{g_i}^f) - h^\nu(T_{g_i})] + \dot{m}_{g_i}^a \sum_{\nu \in G} w_{g_i}^{a,\nu} [h^\nu(T_{g_i}^a) - h^\nu(T_{g_i})]. \quad (8)$$

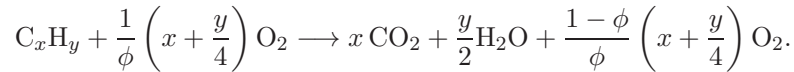
Here, ideal mixing conditions are assumed, i.e.  $w_{g_i}^{out,\nu} = w_{g_i}^\nu$  for all  $\nu \in G$  and  $T_{g_i}^{out} = T_{g_i}$ . Combining (3) and (8) results in a system of ODEs constituting the dynamics of the temperature  $T_{g_i}$  and the composition  $w_{g_i}^\nu$  of the exhaust gas inside the  $i$ -th control volume as a function of the incoming mass flows, their compositions and temperatures, the heat exchange term  $\dot{Q}_{g_i}$ , and the generation rate  $\dot{r}_{g_i}^\nu$ . The latter can be determined from the kinetics of the chemical reactions of the combustion process.

<sup>1</sup>The absolute or standardized enthalpy takes into account the energy associated with chemical bonds and additionally an enthalpy associated only with a change of temperature [11]. This simplifies our notation of energy balances concerning the released combustion heat.

For this, the subsequent analysis is limited to the global reactions of fuel and oxygen under the assumption of lean combustion while neglecting dissociation and the unimolecular reaction mechanism involving intermediate reaction schemes and the generation of radicals. Lean combustion thereby denotes the fact that more oxygen is supplied than required for a stoichiometric reaction in contrast to the so-called rich combustion where less oxygen is supplied. Hence it seems adequate to consider a complete oxidization of the elements of  $G_o$ . By employing so-called net rates of production or destruction (cf. [11, p. 119f]), the mass generation rates  $\dot{r}_{g_i}^\nu$  for  $\nu \in G$  can be determined schematically as follows

$$\dot{r}_{g_i}^\nu = \begin{cases} -\bar{\chi}_\nu^\nu K^\nu(T_{g_i})(c_{g_i}^\nu)^{\gamma_\nu^\nu} (c_{g_i}^{O_2})^{\gamma_{O_2}^\nu} & \text{for } \nu \in G_o \\ \sum_{\mu \in G_o} \bar{\chi}_\nu^\mu K^\mu(T_{g_i})(c_{g_i}^\mu)^{\gamma_\mu^\nu} (c_{g_i}^{O_2})^{\gamma_{O_2}^\mu} & \text{for } \nu \in G_e \cup \{O_2\} \\ 0 & \text{else} \end{cases} \quad (9)$$

with the modified stoichiometric coefficients  $\bar{\chi}_\nu^\mu = \chi_\nu^\mu$  for  $\nu \neq O_2$  and  $\bar{\chi}_{O_2}^\mu = -\phi \chi_{O_2}^\mu$ ,  $\nu \in G_e$  and  $\mu \in G_o$ . Herein  $\chi_\nu^\mu$  denotes the stoichiometric coefficient of the component  $\nu \in G$  in the oxidization reaction scheme of the oxidizable component  $\mu \in G_o$ . Note that the destruction of  $O_2$  is incorporated in (9) by the negative sign of the respective modified stoichiometric coefficient  $\bar{\chi}_{O_2}^\mu$  in order to obtain a uniform representation in the subsequent analysis. The parameter  $\phi < 1$  is called the equivalence ratio indicating that the fuel-oxygen mixture is lean,  $K^\nu(T_{g_i})$ ,  $\nu \in G$  is called the global rate coefficient, and  $c_{g_i}^\nu$  denotes the molar concentration of the component  $\nu \in G$  in the  $i$ -th gas volume. Finally, the exponents  $\gamma_\nu^\mu$  can be either fitted to experimental data or determined from the chemical kinetics by employing collision theory. For the first case, tabulated values can be, e.g., found in [11, Table 5.1]. In the second case, consider the example when  $G_o$  consists only of hydrocarbon-type elements, i.e.  $C_xH_y \in G_o$  with  $x \in \mathbb{N} \cup \{0\}$ ,  $y \in \mathbb{N}$  denoting the number of carbon and hydrogen atoms, respectively. The respective global reaction scheme in case of lean combustion follows as



Then, the kinetic coefficients in (9) can be identified as

$$\begin{aligned} \chi_{C_xH_y}^{C_xH_y} &= \gamma_{C_xH_y}^{C_xH_y} = 1, & \chi_{O_2}^{C_xH_y} &= \gamma_{O_2}^{C_xH_y} = \frac{1}{\phi} \left( x + \frac{y}{4} \right), \\ \chi_{CO_2}^{C_xH_y} &= \gamma_{CO_2}^{C_xH_y} = x, & \chi_{H_2O}^{C_xH_y} &= \gamma_{H_2O}^{C_xH_y} = \frac{y}{2} \end{aligned}$$

with  $G_e = \{CO_2, H_2O\}$ . It should be pointed out that by the choice of an adequate generation rate  $\dot{r}_{g_i}^\nu$  and an associated set  $G_e$  it is possible to incorporate the full reaction kinetics with dissociation, incomplete combustion, and effects such as steel oxidization. For more details on the analysis of combustion processes, the reader is referred to [11].

Note that the molar concentrations in (9) can be expressed in terms of mass fractions by utilizing the relation  $c_{g_i}^\nu = w_{g_i}^\nu m_{g_i} / (V_{g_i} M^\nu)$  such that substitution of (9) into (3) yields three sets of ODEs with the

first two sets being coupled by the reaction rates, i.e.

$$m_{g_i} \frac{dw_{g_i}^\nu}{dt} = \dot{m}_{g_i}^{in} \left( w_{g_i}^{in,\nu} - w_{g_i}^\nu \right) + \dot{m}_{g_i}^b \left( w_{g_i}^{b,\nu} - w_{g_i}^\nu \right) - V_{g_i} M^\nu \bar{\chi}_\nu^\nu \bar{K}^\nu(T_{g_i}) (w_{g_i}^\nu)^{\gamma_\nu^\nu} (w_{g_i}^{O_2})^{\gamma_{O_2}^\nu}, \quad \nu \in G_o \quad (10a)$$

$$m_{g_i} \frac{dw_{g_i}^\nu}{dt} = \dot{m}_{g_i}^{in} \left( w_{g_i}^{in,\nu} - w_{g_i}^\nu \right) + \dot{m}_{g_i}^b \left( w_{g_i}^{b,\nu} - w_{g_i}^\nu \right) + V_{g_i} M^\nu \sum_{\mu \in G_o} \bar{\chi}_\nu^\mu \bar{K}^\mu(T_{g_i}) (w_{g_i}^\mu)^{\gamma_\mu^\mu} (w_{g_i}^{O_2})^{\gamma_{O_2}^\mu}, \quad \nu \in G_e \cup \{O_2\} \quad (10b)$$

$$m_{g_i} \frac{dw_{g_i}^\nu}{dt} = \dot{m}_{g_i}^{in} \left( w_{g_i}^{in,\nu} - w_{g_i}^\nu \right) + \dot{m}_{g_i}^b \left( w_{g_i}^{b,\nu} - w_{g_i}^\nu \right), \quad \nu \in G_n \quad (10c)$$

where  $G_n = G \setminus (G_o \cup G_e \cup \{O_2\})$  denotes the non-reactive components such as  $N_2$ . Here the abbreviation  $\bar{K}^\nu(T_{g_i}) = K^\nu(T_{g_i}) (m_{g_i}/V_{g_i})^{\gamma_\nu^\nu + \gamma_{O_2}^\nu} (M^\nu)^{-\gamma_\nu^\nu} (M^{O_2})^{-\gamma_{O_2}^\nu}$  is used, where  $\bar{K}^\nu(T_{g_i})$  now depends on the mass fractions of all components in  $G$  due to (4).

Since the pressure  $p$  inside the furnace and the volume  $V_{g_i}$  of the  $i$ -th control volume are known the mass  $m_{g_i}$  can be determined algebraically from (4) for given  $w_{g_i}^\nu$  and  $T_{g_i}$ . Thus, utilizing (4) the gas dynamics of the  $i$ -th control volume is given by the exhaust gas composition from (10) and the exhaust gas temperature from (8) with (9). Note that due to the assumption of a well stirred control volume these ODEs are independent from the outgoing exhaust gas mass flow  $\dot{m}_{g_i}^{out}$  which can be determined from (1) with (4) for known  $w_{g_i}^\nu$  and  $T_{g_i}$  as mentioned before.

It should be noted that the combustion reaction included in (8) and (10a), (10b), respectively, represents a very fast dynamics compared to the rather slow mass diffusion through the volume. Since it is desired to obtain a model suitable for the development of model-based real-time control and observation strategies, it is adequate to assume a quasi-instantaneous reaction of all oxidizable fuel components  $G_o$  with  $O_2$ . This results in a systematic model reduction by applying singular perturbation techniques (cf. [13]) as presented in the following section.

## 2.2. Reduced gas dynamics by singular perturbation

In order to eliminate the fast dynamics of the combustion process represented by  $K^\nu(T_{g_i}) \rightarrow \infty$  or respectively  $\bar{K}^\nu(T_{g_i}) \rightarrow \infty$ , singular perturbation theory is applied with respect to the small parameter  $1/\bar{K}^\nu(T_{g_i})$ . For this, the ODEs (8) and (10) have to be transformed into singular perturbation standard form. For the transformation of the governing equation (10) we introduce the new states  $\tilde{w}_{g_i}^\nu = w_{g_i}^\nu + \sum_{\mu \in G_o} \beta_\nu^\mu w_{g_i}^\mu$  for all  $\nu \in G_e \cup \{O_2\}$  where  $\beta_\nu^\mu = M^\nu \bar{\chi}_\nu^\mu / (M^\mu \bar{\chi}_\mu^\mu)$ . Note that this state transformation corresponds to the summation of (10a) weighted by  $\beta_\nu^\mu$  with respect to  $\mu \in G_o$  and the addition of the result to (10b). This yields

$$m_{g_i} \frac{d\tilde{w}_{g_i}^\nu}{dt} = \dot{m}_{g_i}^{in} \left( w_{g_i}^{in,\nu} + \sum_{\mu \in G_o} \beta_\nu^\mu w_{g_i}^{in,\mu} - \tilde{w}_{g_i}^\nu \right) + \dot{m}_{g_i}^b \left( w_{g_i}^{b,\nu} + \sum_{\mu \in G_o} \beta_\nu^\mu w_{g_i}^{b,\mu} - \tilde{w}_{g_i}^\nu \right), \quad \nu \in G_e \cup \{O_2\}, \quad (11)$$

which is independent of  $\bar{K}^\nu(T_{g_i})$ . This state transformation applied to (8) is more involved and leads to the enthalpy conservation (5) which is also independent of  $\bar{K}^\nu(T_{g_i})$ . Hence, starting with this equation the resulting system consisting of (5)-(7), (10a), (10c), and (11) is in singular perturbation standard form with respect to the parameter  $1/\bar{K}^\nu(T_{g_i})$  when dividing both sides of (10a) by  $\bar{K}^\nu(T_{g_i})$ .

By taking the limit  $1/\bar{K}^\nu(T_{g_i}) \rightarrow 0$ , it follows from (10a) that  $w_{g_i}^\nu = 0$  for all  $\nu \in G_o$  since due to the

assumption of lean combustion necessarily  $w_{g_i}^{O_2} > 0$ . With this result, (11) evaluates to

$$m_{g_i} \frac{dw_{g_i}^\nu}{dt} = \dot{m}_{g_i}^{in} \left( w_{g_i}^{in,\nu} - w_{g_i}^\nu \right) + \dot{m}_{g_i}^b \left( w_{g_i}^{b,\nu} - w_{g_i}^\nu \right) + \sum_{\mu \in G_o} \beta_\nu^\mu \left( \dot{m}_{g_i}^{in} w_{g_i}^{in,\mu} + \dot{m}_{g_i}^b w_{g_i}^{b,\mu} \right), \quad \nu \in G_e \cup \{O_2\} \quad (12)$$

while the energy balance (5)-(7) yields

$$m_{g_i} c_{p,g_i} \frac{dT_{g_i}}{dt} = -\dot{Q}_{g_i} + \dot{m}_{g_i}^f h_{g_i}^f + \dot{m}_{g_i}^a h_{g_i}^a + \dot{m}_{g_i}^{in} h_{g_i}^{in} - \sum_{\nu \in G_e \cup G_a} h^\nu(T_{g_i}) \bar{w}_{g_i}^\nu - \sum_{\nu \in G_e \cup \{O_2\}} h^\nu(T_{g_i}) \sum_{\mu \in G_o} \beta_\nu^\mu \bar{w}_{g_i}^\mu \quad (13)$$

where  $h_{g_i}^f = \sum_{\nu \in G_f} w_{g_i}^{f,\nu} h^\nu(T_{g_i}^f)$ ,  $h_{g_i}^a = \sum_{\nu \in G_a} w_{g_i}^{a,\nu} h^\nu(T_{g_i}^a)$ ,  $h_{g_i}^{in} = \sum_{\nu \in G_e \cup G_a} w_{g_i}^{in,\nu} h^\nu(T_{g_i}^{in})$ , and  $\bar{w}_{g_i}^\nu = \dot{m}_{g_i}^f w_{g_i}^{f,\nu} + \dot{m}_{g_i}^a w_{g_i}^{a,\nu} + \dot{m}_{g_i}^{in} w_{g_i}^{in,\nu}$ . Note that since  $w_{g_i}^\nu = 0$  for all  $\nu \in G_o$  the set  $G$  reduces to  $G = G_e \cup G_a$ .

In summary, combining (10c), (12) and (13) results in a coupled system of ODEs representing the reduced gas dynamics of the  $i$ -th control volume, i.e. the exhaust gas composition represented by the component mass fractions and the gas temperature, in the form

$$\frac{d}{dt} \begin{bmatrix} \mathbf{w}_{g_i} \\ T_{g_i} \end{bmatrix} = \begin{bmatrix} \mathbf{f}_{\mathbf{w}_{g_i}}(\mathbf{w}_{g_i}, T_{g_i}, \mathbf{w}_{g_i}^{in}, \dot{m}_{g_i}^{in}, \mathbf{u}_{g_i}) \\ f_{T_{g_i}}(\mathbf{w}_{g_i}, T_{g_i}, \mathbf{w}_{g_i}^{in}, T_{g_i}^{in}, \dot{m}_{g_i}^{in}, \mathbf{u}_{g_i}, \dot{Q}_{g_i}) \end{bmatrix} \quad (14)$$

for  $t > 0$  and initial condition  $[\mathbf{w}_{g_i}^T, T_{g_i}]^T(0) = [(\mathbf{w}_{g_i}^0)^T, T_{g_i}^0]^T$ . Here, the mass fractions of the exhaust gases inside the  $i$ -th control volume are summarized in the state vector  $\mathbf{w}_{g_i}$ , i.e.  $\mathbf{w}_{g_i} = \{w_{g_i}^\nu\}_{\nu \in G_e \cup G_a}$ . Similar to this, the composition of the incoming mass flow  $\dot{m}_{g_i}^{in}$  is summarized in the vector of mass fractions  $\mathbf{w}_{g_i}^{in} = \{w_{g_i}^{in,\nu}\}_{\nu \in G_e \cup G_a}$ . Furthermore, the mass flows of fuel and combustion air into the control volume as well as their compositions and temperatures constitute the input quantities of the  $i$ -th control volume. Hence, they are combined in the input vector  $\mathbf{u}_{g_i} = [(\mathbf{w}_{g_i}^f)^T, (\mathbf{w}_{g_i}^a)^T, T_{g_i}^f, T_{g_i}^a, \dot{m}_{g_i}^f, \dot{m}_{g_i}^a]^T$  with the vector of mass fractions of the fuel gas  $\mathbf{w}_{g_i}^f = \{w_{g_i}^{f,\nu}\}_{\nu \in G_e \cup G_a}$  and the combustion air  $\mathbf{w}_{g_i}^a = \{w_{g_i}^{a,\nu}\}_{\nu \in G_e \cup G_a}$ . In addition, recall that the mass flow within the furnace is dominated by the flow which is directed towards the funnel. Therefore, the mass flow leaving the  $i$ -th control volume enters the adjacent control volume, i.e.  $\dot{m}_{g_i}^{out} = \dot{m}_{g_{i-1}}^{in}$  (cf. Figure 3). Additionally, the outgoing mass flow can be represented schematically as

$$\dot{m}_{g_i}^{out} = f_{g_i}^{out}(\mathbf{w}_{g_i}, T_{g_i}, \mathbf{w}_{g_i}^{in}, T_{g_i}^{in}, \dot{m}_{g_i}^{in}, \mathbf{u}_{g_i}, \dot{Q}_{g_i}) \quad (15)$$

utilizing (2) and (4) as mentioned before. The temperature evolution as well as the gas composition of the  $i$ -th control volume is given by (14) depending on the heat flow  $\dot{Q}_{g_i}$  out of the control volume. This heat flow summarizes the heat exchange of the exhaust gas with the furnace walls and the slabs which is modelled in the following.

### 2.3. Dynamics of the furnace wall

The walls of modern furnaces are normally piled up of several levels of various insulation materials embedded in an exterior shell of steel as schematically shown in Figure 4(a). The thermal properties of the individual layers are given by the material dependent heat capacity  $c_{p,w_i}^n$  and density  $\rho_{w_i}^n$  where  $1 \leq n \leq n_{w_i}$

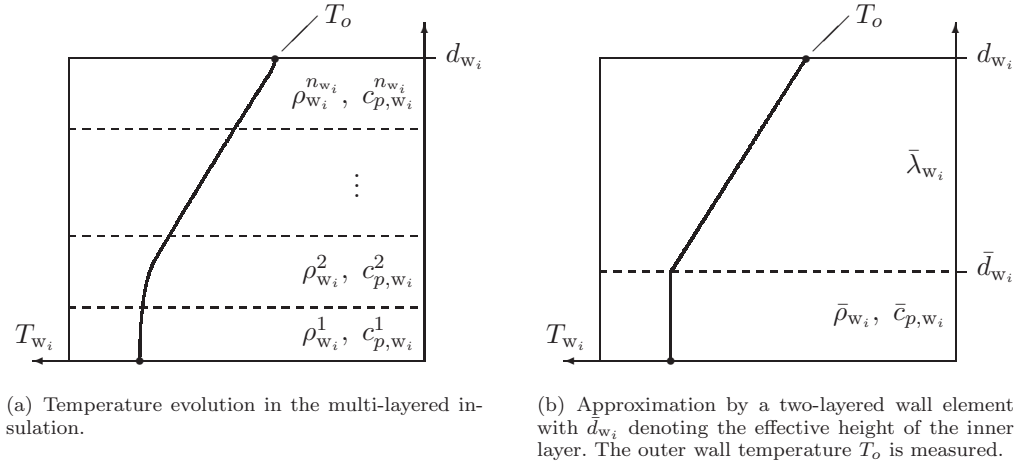


Figure 4. Modelling of the furnace wall  $w_i$  in the  $i$ -th control volume.

indicates the respective layer. In order to model the temperature distribution in the furnace wall the convective as well as conductive heat transfer mechanisms have to be considered [14]. However, since on the one hand the convective flow in the furnace is hardly accessible due to the complex furnace dynamics and geometry and on the other hand the conductive properties of the multiple insulation layers are mainly unknown, an adapted model has to be derived, which captures the essential thermal dynamics.

For this, detailed simulation studies in comparison with measurement campaigns have shown that the wall temperature mainly varies in a rather thin boundary layer neighbouring the gaseous space followed by an almost linear decrease to the outer wall temperature. As a result, in the following the multi-layered wall of area  $A_{w_i}$  and thickness  $d_{w_i}$  surrounding the  $i$ -th control volume is represented by a two-layered element as depicted in Figure 4(b). The balance of energy for the inner layer of effective thickness  $\bar{d}_{w_i} \ll d_{w_i}$ , mean density  $\bar{\rho}_{w_i}$  and mean specific heat capacity  $\bar{c}_{p,w_i}$  reads as

$$\frac{d}{dt} T_{w_i} = \frac{\dot{Q}_{w_i} - \dot{Q}_{w_i}^{out}}{\bar{c}_{p,w_i} \bar{\rho}_{w_i} A_{w_i} \bar{d}_{w_i}}, \quad (16)$$

with the heat flow  $\dot{Q}_{w_i}$  entering the wall and  $\dot{Q}_{w_i}^{out}$  the heat flow to the outer layer. Note that the description of the heat flow  $\dot{Q}_{w_i}$  is postponed to Section 3, where heat radiation in the furnace as the major mode of heat exchange between the gaseous phase, the slabs, and the walls is discussed in detail. The heat flow  $\dot{Q}_{w_i}^{out}$  due to heat conduction follows as

$$\dot{Q}_{w_i}^{out} = \frac{\bar{\lambda}_{w_i} A_{w_i}}{d_{w_i} - \bar{d}_{w_i}} (T_{w_i} - T_o), \quad (17)$$

where  $\bar{\lambda}_{w_i}$  denotes the average thermal conductivity of the outer layer and  $T_o$  represents the outer wall temperature [14, 15]. It should be pointed out, that  $T_o$  is measured in the considered furnace set-up while the parameters  $\bar{d}_{w_i} \ll d_{w_i}$ ,  $\bar{\rho}_{w_i}$ ,  $\bar{c}_{p,w_i}$ , and  $\bar{\lambda}_{w_i}$  are identified from experimental data.

Besides the balance equations for the gaseous furnace space and the surrounding furnace walls, the modelling of the slabs is of crucial importance.

#### 2.4. Dynamics of the slabs

In pusher-type furnaces, the slab movement in the  $z$ -direction is realized by hydraulic pushers, which discontinuously feed new slabs to the furnace. This results in a sliding of the adjoining slabs along the installed skid system as depicted in Figure 5.

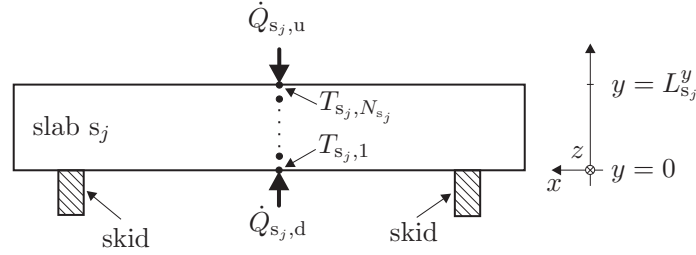


Figure 5. Schematic drawing of the  $j$ -th slab, the vertical discretization and the heat flow into the upper and lower surfaces of the slab.

From an energetic point of view, the skids induce a complex temperature distribution in the slab, which can be mathematically recovered only by considering 2- (along the  $(x, y)$ -directions) or 3-dimensional slab models, see, e.g., [16]. However, a detailed slab model results in a dramatic increase in the dimension of the system states and thus cannot be used in a real-time environment. Furthermore, in view of process control no active control of the slab temperature in the neighbourhood of the skids is available, such that in the sequel the analysis is restricted to a 1-dimensional slab model assuming a homogeneous temperature distribution in the  $x$ - and  $z$ -direction. In addition, it is assumed that the heat exchange occurs mainly through the upper and lower surfaces of the slabs. Note that these assumptions are in good agreement with the available measurement data (cf. Section 5). Hence, the temperature distribution  $T_{s_j} = T_{s_j}(t, y)$  of the  $j$ -th slab  $s_j$  can be represented by the 1-dimensional heat equation [14], i.e.

$$c_{p,s_j}(T_{s_j})\rho_{s_j}(T_{s_j})\frac{\partial T_{s_j}}{\partial t} = \frac{\partial}{\partial y} \left( \lambda_{s_j}(T_{s_j}) \frac{\partial T_{s_j}}{\partial y} \right) \quad (18)$$

with the temperature dependent parameters for the specific heat capacity  $c_{p,s_j}$ , the density  $\rho_{s_j}$ , and the thermal conductivity  $\lambda_{s_j}$  of the respective steel alloy [17]. The boundary conditions follow as

$$\lambda_{s_j}(T_{s_j}) \frac{\partial T_{s_j}}{\partial y} = - \frac{\dot{Q}_{s_j,d}}{A_{s_j}} \quad \text{at } y = 0 \quad (19a)$$

$$\lambda_{s_j}(T_{s_j}) \frac{\partial T_{s_j}}{\partial y} = \frac{\dot{Q}_{s_j,u}}{A_{s_j}} \quad \text{at } y = L_{s_j}^y. \quad (19b)$$

Here  $\dot{Q}_{s_j,d}$  and  $\dot{Q}_{s_j,u}$  denote the heat flows into the slab  $s_j$  at the upper and lower slab surface  $A_{s_j}$ , which depend on the properties of the surrounding gas and the neighbouring furnace walls due to the dominating radiative heat exchange. A detailed derivation of the respective expressions for  $\dot{Q}_{s_j,d}$  and  $\dot{Q}_{s_j,u}$  is given in Section 3. The corresponding initial conditions read as

$$T_{s_j}(t_0, y) = T_{s_j}^0(y), \quad y \in [0, L_{s_j}^y]. \quad (20)$$

with  $t_0 \geq 0$  as the charging time of the respective slab.

In order to obtain a model suitable for real-time applications the governing heat equation (18) and the corresponding boundary conditions (19) are semi-discretized using the finite difference method [14, 18]. This results in a system of  $N_{s_j}$  nonlinear ODEs

$$\frac{d}{dt} \mathbf{T}_{s_j} = \mathbf{f}_{s_j} \left( \mathbf{T}_{s_j}, \dot{Q}_{s_j,d}, \dot{Q}_{s_j,u} \right) \quad (21a)$$

for  $t > t_0$  with the initial condition  $\mathbf{T}_{s_j}(t_0) = \mathbf{T}_{s_j}^0$  due to (20). Thus, a nonlinear system of ODEs with the state vector  $\mathbf{T}_{s_j}(t) = [T_{s_j,1}, \dots, T_{s_j,N_{s_j}}]^T$  of discrete slab temperatures along the slab height as depicted in Figure 5 is obtained for each slab. The following section is devoted to the derivation of the heat flows  $\dot{Q}_{s_j,u}$  and  $\dot{Q}_{s_j,d}$  as well as of the heat flows into the furnace walls  $\dot{Q}_{w_i}$  and out of the exhaust gas  $\dot{Q}_{g_i}$ .

### 3. Heat radiation within the furnace

In the previous section, dynamical models are determined for the exhaust gas composition and the exhaust gas temperature as well as for the wall and the slab temperature distributions. Herein, the heat flows entering or leaving the sub-models are represented schematically by the variables  $\dot{Q}_{g_i}$ ,  $\dot{Q}_{w_i}$ ,  $\dot{Q}_{s_j,u}$ , and  $\dot{Q}_{s_j,d}$ . Basically, these heat flows are caused by an energy exchange between the exhaust gas, the walls and the slabs. Since the pusher-type furnace is normally operated at temperatures above 1000°C, radiative heat exchange is considered as the major mode of heat exchange such that convective heat exchange between the gas phase and the wall and the slab surfaces can be neglected. Next the radiative heat transfer mechanisms inside a fuel fired furnace will be briefly outlined followed by the determination of the heat flows  $\dot{Q}_{g_i}$ ,  $\dot{Q}_{w_i}$ ,  $\dot{Q}_{s_j,u}$ , and  $\dot{Q}_{s_j,d}$ .

#### 3.1. Radiating properties

For the subsequent derivations solid body and gas radiation have to be distinguished. Thereby, the solid surfaces of the furnace walls and the slabs are considered as diffuse, opaque, and grey radiators. The emissivity of solid surfaces depends among others on the surface temperature, the material, and the surface texture. For the slabs the latter is affected by the proceeding surface oxidization during the reheating process<sup>1</sup>, which significantly complicates the determination of the emissivity of the slabs or makes it even impossible. Hence, in the following an empirical surface temperature dependent emissivity  $\varepsilon_{s_j}(T_{s_j,1})$  and  $\varepsilon_{s_j}(T_{s_j,N_{s_j}})$  is presumed. Since the temperature of the furnace walls only varies in a small temperature range the emissivity of the furnace walls  $\varepsilon_{w_i}$  is considered constant.

The heat radiation of the exhaust gas in general is caused by the polar elements in  $G_e$ , i.e. in our case CO<sub>2</sub> and H<sub>2</sub>O, whereas the radiating properties of these gases primarily depend on their temperature  $T_{g_i}$  as well as on the volume and the shape of the radiating gas space. The latter is approximated by the mean beam length  $l_{g_i}^* = 3.6V_{g_i}/A_{g_i}$  where  $V_{g_i}$  denotes the volume of the  $i$ -th control volume and  $A_{g_i}$  corresponds to its surrounding area [14]. The gas radiation properties also depend on the chemical composition of the gas phase, which is incorporated in the partial pressures  $p_{g_i}^{\text{CO}_2}$  and  $p_{g_i}^{\text{H}_2\text{O}}$  of the radiating gases, i.e.

$$p_{g_i}^{\text{CO}_2} = \frac{w_{g_i}^{\text{CO}_2} p}{M_{\text{CO}_2} \sum_{\nu \in G_a \cup G_e} \frac{w_{g_i}^{\nu}}{M_{\nu}}}, \quad p_{g_i}^{\text{H}_2\text{O}} = \frac{w_{g_i}^{\text{H}_2\text{O}} p}{M_{\text{H}_2\text{O}} \sum_{\nu \in G_a \cup G_e} \frac{w_{g_i}^{\nu}}{M_{\nu}}} \quad (22)$$

such that  $\varepsilon_{g_i}^{\nu} = \varepsilon_{g_i}^{\nu}(T_{g_i}, p, p_{g_i}^{\nu}, l_{g_i}^*)$  with  $\nu \in \{\text{CO}_2, \text{H}_2\text{O}\}$ . The determination of  $\varepsilon_{g_i}^{\text{CO}_2}$  and  $\varepsilon_{g_i}^{\text{H}_2\text{O}}$  is typically based on the measured diagrams of Hottel and Egbert [20] which relate the gas emissivities to the gas temperature and the product of the respective partial pressure and the mean beam length, i.e.  $\varepsilon_{g_i}^{\nu} = \varepsilon_{g_i}^{\nu}(T_{g_i}, l_{g_i}^* p_{g_i}^{\nu})$  for  $\nu \in \{\text{CO}_2, \text{H}_2\text{O}\}$ . For a detailed discussion of this subject the reader is referred to [14,20]. Furthermore, the emissivity of the radiating atmosphere inside the  $i$ -th control volume is assumed to follow from the emissivity of carbon dioxide  $\varepsilon_{g_i}^{\text{CO}_2}$  and  $\varepsilon_{g_i}^{\text{H}_2\text{O}}$ , i.e.

$$\varepsilon_{g_i}(T_{g_i}, \mathbf{w}_{g_i}) = \varepsilon_{g_i}^{\text{CO}_2}(T_{g_i}, l_{g_i}^* p_{g_i}^{\text{CO}_2}) + \varepsilon_{g_i}^{\text{H}_2\text{O}}(T_{g_i}, l_{g_i}^* p_{g_i}^{\text{H}_2\text{O}}) - \Delta\varepsilon_{g_i}(T_{g_i}, p_{g_i}^{\text{CO}_2}, p_{g_i}^{\text{H}_2\text{O}}, l_{g_i}^*) \quad (23a)$$

as given in [14]. The correction term  $\Delta\varepsilon_{g_i}$  takes into account weakening effects of the radiation caused by the partially overlapping radiation spectra of CO<sub>2</sub> and H<sub>2</sub>O. In order to calculate  $\varepsilon_{g_i}$  numerically, in the following the approximations of the diagrams from Hottel and Egbert [20] as proposed in [21] are applied. The calculation of the exhaust gas absorptivity  $\alpha_{g_i}$  is more involved than the determination of  $\varepsilon_{g_i}$  because  $\alpha_{g_i}$  additionally depends on the temperature of the radiation emitting surface or gas  $T_{\text{sender}}$ . Hottel and

<sup>1</sup>The oxidization kinetic depends among others on the surface temperature of the slab and the composition and temperature of the furnace atmosphere and is not considered in this contribution. Further information on this topic can be found in [19].

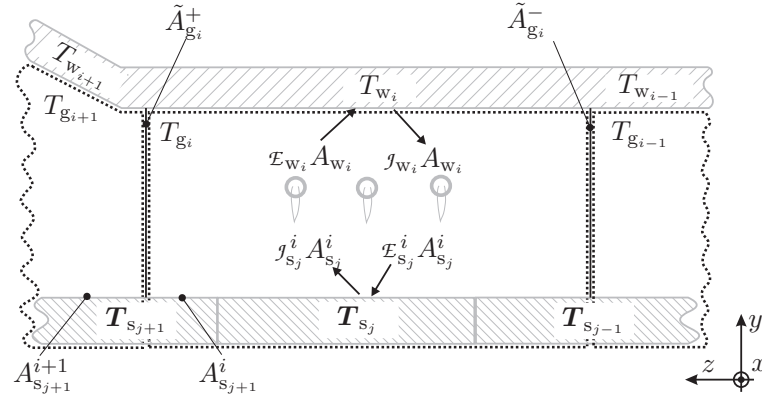


Figure 6. Schematic diagram of the emitted and received radiation for the surrounding wall of the  $i$ -th control volume and the  $j$ -th slab.

Egbert [14,20] relate the absorptivity to the emissivity in the form

$$\alpha_{g_i}(T_{g_i}, \mathbf{w}_{g_i}, T_{\text{sender}}) = \left( \frac{T_{g_i}}{T_{\text{sender}}} \right)^{0.65} \varepsilon_{g_i}^{\text{CO}_2} \left( T_{g_i}, l_{g_i}^* p_{g_i}^{\text{CO}_2} \frac{T_{\text{sender}}}{T_{g_i}} \right) + \left( \frac{T_{g_i}}{T_{\text{sender}}} \right)^{0.45} \varepsilon_{g_i}^{\text{H}_2\text{O}} \left( T_{g_i}, l_{g_i}^* p_{g_i}^{\text{H}_2\text{O}} \frac{T_{\text{sender}}}{T_{g_i}} \right) - \Delta\alpha_{g_i} \quad (23b)$$

with  $\Delta\alpha_{g_i} = \Delta\varepsilon_{g_i}$ . Note that for the calculation of the absorptivity we do not distinguish between the gray radiation emitted from a solid surface and the radiation reflected by gray surfaces after several passes through the gas phase or the radiation initially emitted by a gas, i.e. radiation composed of different spectral distributions. However, as long as the reflected radiation is rather small, i.e.  $\varepsilon_{s_j}$  and  $\varepsilon_{w_i}$  are close to unity, this approximation is sufficiently accurate. As a consequence, the transmissivity of the gas phase is introduced as  $\tau_{g_i}(T_{g_i}, \mathbf{w}_{g_i}, T_{\text{sender}}) = 1 - \alpha_{g_i}(T_{g_i}, \mathbf{w}_{g_i}, T_{\text{sender}})$ . In view of a compact notation, in the following the arguments of  $\varepsilon_{g_i}$  and  $\alpha_{g_i}$  are neglected whenever they are self-explanatory and additionally the abbreviations  $\tau_{g_i}^{g_k} = \tau_{g_i}(T_{g_i}, \mathbf{w}_{g_i}, T_{g_k})$ ,  $\tau_{g_i}^{w_k} = \tau_{g_i}(T_{g_i}, \mathbf{w}_{g_i}, T_{w_k})$  and  $\tau_{g_i}^{s_j} = \tau_{g_i}(T_{g_i}, \mathbf{w}_{g_i}, T_{s_j})$  are introduced for the transmissivity of the control volume  $i$  for radiation emitted by the control volume  $g_k$ ,  $k = 1, \dots, 2N_v$  and  $k \neq i$ , the wall  $w_k$ ,  $k = 1, \dots, 2N_v$ , and the slab  $s_j$ ,  $j = 1, \dots, N_{\text{slab}}$ , respectively. For more detailed information on this topic the reader is referred to [14,22].

### 3.2. Heat flow determination

In the following the determination of the heat flows  $\dot{Q}_{g_i}$ ,  $\dot{Q}_{w_i}$ ,  $\dot{Q}_{s_j,u}$  and  $\dot{Q}_{s_j,d}$  in (13), (16), and (21) is outlined. For this, the configuration illustrated in Figure 6 is considered and energy balances according to the net-radiation method (cf. [14]) are applied. Furthermore, it is assumed that the part of the separation plane between the upper and lower furnace section which is not obstructed by slabs is rather small. Hence, the radiative heat exchange between the upper and lower furnace sections is neglected and thus the radiative heat transfer for each section is derived separately. In the following the upper furnace section as shown in Figure 6 is considered, i.e.  $i = 1, \dots, N_v$ , and radiative balances are applied for each volume and each surface with homogeneous temperature inside the volumes. For this, the slab surfaces not fully included in a control volume, e.g., the  $s_{j-1}$ -th and  $s_{j+1}$ -th slab in Figure 6, are subdivided into surface parts each entirely located inside the respective control volumes. Thus, the surface  $A_{s_{j+1}}$  of slab  $s_{j+1}$  is subdivided into the area  $A_{s_{j+1}}^i$  located in the  $i$ -th control volume and the area  $A_{s_{j+1}}^{i+1}$  located in the  $(i+1)$ -th control volume, i.e.  $A_{s_j} = \sum_{i=1}^{N_v} A_{s_j}^i$  where  $A_{s_j}^i \neq 0$  if the slab  $s_j$  is at least partly located in the volume  $i = 1, \dots, N_v$  while else  $A_{s_j}^i = 0$ .

Energy balancing for the wall  $w_i$  and the slab  $s_j$ , respectively, yields

$$\dot{Q}_{w_i} = \mathcal{E}_{w_i} A_{w_i} - \mathcal{J}_{w_i} A_{w_i}, \quad \dot{Q}_{s_j, u} = \sum_{i=1}^{N_v} \left( \mathcal{E}_{s_j}^i A_{s_j}^i - \mathcal{J}_{s_j}^i A_{s_j}^i \right), \quad (24)$$

where  $\mathcal{E}_{w_i} A_{w_i}$  and  $\mathcal{E}_{s_j}^i A_{s_j}^i$  denote the irradiance received by the surfaces  $A_{w_i}$  and  $A_{s_j}^i$  while  $\mathcal{J}_{w_i} A_{w_i}$  and  $\mathcal{J}_{s_j}^i A_{s_j}^i$  are called the radiosity of the surfaces  $A_{w_i}$  and  $A_{s_j}^i$ , respectively. Furthermore, the radiosity is composed of the emissive power of the respective surface and the portion of reflected irradiance, i.e.

$$\mathcal{J}_{w_i} A_{w_i} = \sigma \varepsilon_{w_i} A_{w_i} T_{w_i}^4 + (1 - \varepsilon_{w_i}) \mathcal{E}_{w_i} A_{w_i} \quad (25a)$$

$$\mathcal{J}_{s_j}^i A_{s_j}^i = \sigma \varepsilon_{s_j} A_{s_j}^i T_{s_j, N_{s_j}}^4 + (1 - \varepsilon_{s_j}) \mathcal{E}_{s_j}^i A_{s_j}^i \quad (25b)$$

with  $\sigma$  the Stefan–Boltzmann constant (cf. [14]). The irradiance is represented by the received radiosity of all surfaces in the upper furnace section and the emissive power of the gas volumes weighted with the respective transmissivity, i.e.

$$\mathcal{E}_{w_i} A_{w_i} = \sum_{k=1}^{N_v} \left[ \mathcal{J}_{w_k} A_{w_k} F_{A_{w_k}, A_{w_i}} \tilde{\tau}_{k,i}^{w_k} + \sigma \varepsilon_{g_k} \kappa_{i,k}^{A_{w_i}, g_k} T_{g_k}^4 + \sum_{j=1}^{N_{\text{slab}}} \mathcal{J}_{s_j}^k A_{s_j}^k F_{A_{s_j}^k, A_{w_i}} \tilde{\tau}_{k,i}^{s_j} \right] \quad (26a)$$

$$\mathcal{E}_{s_j}^i A_{s_j}^i = \sum_{k=1}^{N_v} \left[ \mathcal{J}_{w_k} A_{w_k} F_{A_{w_k}, A_{s_j}^i} \tilde{\tau}_{k,i}^{w_k} + \sigma \varepsilon_{g_k} \kappa_{i,k}^{A_{s_j}^i, g_k} T_{g_k}^4 \right]. \quad (26b)$$

Thereby, the orientation of the surfaces  $A_1$  and  $A_2$  is taken into account by the so-called view factor  $F_{A_1, A_2}$  relating the portion of the radiosity emitted by the surface  $A_1$  being received by the surface  $A_2$  (cf. [14]). Assuming planar surfaces, the view factors can easily be calculated using the algorithms presented in [22, 23]. Additionally, the abbreviations

$$\tilde{\tau}_{k,i}^l = \begin{cases} \prod_{\varrho=k}^i \tau_{g_\varrho}^l & \text{for } i > k \\ \tau_{g_i}^l & \text{for } i = k \\ \prod_{\varrho=i}^k \tau_{g_\varrho}^l & \text{for } i < k \end{cases} \quad \text{and} \quad \kappa_{i,k}^{\zeta, \xi} = \begin{cases} \tilde{A}_{g_k}^- F_{\tilde{A}_{g_k}^-, \zeta} \tilde{\tau}_{i,k-1}^{\xi} & \text{for } i < k \\ \zeta & \text{for } i = k \\ \tilde{A}_{g_k}^+ F_{\tilde{A}_{g_k}^+, \zeta} \tilde{\tau}_{i,k+1}^{\xi} & \text{for } i > k \end{cases} \quad (27)$$

are introduced, where  $\tilde{\tau}_{k,i}^l$  combines the transmissivity of the gas volumes  $g_k$  to  $g_i$  due to the radiosity of  $l$ . Note that  $\tilde{A}_{g_i}^+$  and  $\tilde{A}_{g_i}^-$  denote the surface of the separation planes between the  $i$ -th gas volume and the adjacent gas volumes on the left and on the right, respectively (cf. Figure 6). By balancing the emissive power and the absorbed irradiation of the  $i$ -th gas volume, the outgoing heat flow  $\dot{Q}_{g_i}$  follows as

$$\dot{Q}_{g_i} = \sigma \varepsilon_{g_i} A_{g_i} T_{g_i}^4 - \sum_{k=1}^{N_v} \left[ \mathcal{J}_{w_k} \kappa_{k,i}^{A_{w_k}, w_k} \alpha_{g_i}^{w_k} + \sum_{j=1}^{N_{\text{slab}}} \mathcal{J}_{s_j}^k \kappa_{k,i}^{A_{s_j}^k, s_j} \alpha_{g_i}^{s_j} + (1 - \delta_{i,k}) \sigma \varepsilon_{g_k} \alpha_{g_i}^{g_k} \kappa_{k+\text{sign}(i-k), i}^{\tilde{A}_{g_k}^{\text{sign}(i-k)}, g_k} T_{g_k}^4 \right] \quad (28)$$

with the Kronecker delta  $\delta_{i,i} = 1$  while  $\delta_{i,k} = 0$ ,  $i \neq k$  and the signum function  $\text{sign}(i)$ . In order to determine the radiosities  $\mathcal{J}_{w_i}$  and  $\mathcal{J}_{s_j}^i$  for  $i = 1, \dots, N_v$ ,  $j = 1, \dots, N_{\text{slab}}$ , a linear system of equations is obtained by considering (25) with (26) for  $i = 1, \dots, N_v$ ,  $j = 1, \dots, N_{\text{slab}}$ . Furthermore, due to the absorption of the exhaust gas, it makes sense to limit the radiative exchange to adjacent volumes, i.e. to limit the summations in (26) and (28) to  $i - 1 \leq k \leq i + 1$ . This finally allows to compute the remaining heat flows  $\dot{Q}_{s_j, u}$ ,  $\dot{Q}_{w_i}$  and  $\dot{Q}_{g_i}$  of the upper control volumes, walls, and slab surfaces from (24) and (28). Due to the assumption of negligible radiative coupling of the upper and lower furnace sections the heat

flows  $\dot{Q}_{s_j,d}$ ,  $\dot{Q}_{w_i}$  and  $\dot{Q}_{g_i}$  in the lower furnace section are calculated similarly for  $i = N_v + 1, \dots, 2N_v$  and the lower slab temperatures  $T_{s_j,1}$ . The major difference between the furnace sections is the installed skid system consisting of insulated but internally cooled pipes on which the slabs are sliding (cf. Figures 1 and 6). These skids partly obstruct the radiating surfaces, which can be incorporated in the calculation of the respective view factors of the slabs and their environment. Unfortunately, no data is available to identify the spatial cooling characteristics of the skids inside the furnace. Thus, the overall amount of heat dissipated by the skid system is prorated to the lower control volumes and the lower walls. The feasibility of this simplification is shown in Section 5 where the good agreement of simulation results and measurement data are discussed.

#### 4. Model assembling and implementation

In Section 2 dynamical sub-models of the exhaust gas composition and its temperature inside a control volume as well as the temperature of its surrounding wall and the temperature distribution along the height of a slab are determined. These sub-models are coupled by radiative heat transfer as presented in Section 3. Additionally, the control volumes are coupled by the exhaust gas flow. Hence, the determined sub-models for the individual control volumes, wall elements, and slabs can be assembled into a single dynamical system described by a set of coupled nonlinear ODEs. For this, it is assumed that the exhaust gas flow out of a control volume is strictly directed towards the funnel, i.e. along the negative  $z$ -direction and thus this outgoing mass flow enters the adjacent control volume. Hence, it follows that  $\dot{m}_{g_i}^{in} = \dot{m}_{g_{i+1}}^{out}$  and  $T_{g_i}^{in} = T_{g_{i+1}}^{out} = T_{g_{i+1}}$  for  $i = 1, \dots, N_v - 1$  for the upper furnace section and for  $i = N_v + 1, \dots, 2N_v - 1$  for the lower furnace section, respectively, as well as  $\dot{m}_{g_{N_v}}^{in} = \dot{m}_{g_{2N_v}}^{in} = 0$  for the enclosed volumes at the discharging side of the upper and lower furnace parts (cf. Figure 2). Using (15), the mass flow leaving the  $i$ -th control volume  $\dot{m}_{g_i}^{out}$  is calculated by an algebraic equation which can be evaluated in terms of the actual states  $\mathbf{w}_{g_i}$  and  $T_{g_i}$  of the respective volume. Hence, equation (14) can be assembled successively starting with the control volumes  $N_v$  and  $2N_v$  at the discharging side of the furnace (cf. Figure 2). It should be pointed out that in contrast to the modelling of a bidirectional mass exchange of the control volumes, it is not necessary to solve a system of algebraic equations for calculating the mass flow between two control volumes due to the assumption that all mass flows are strictly directed towards the negative  $z$ -direction<sup>1</sup>. Under this assumption, equations (14) and (16) for each control volume and each wall element, respectively, as well as equation (21) for all slabs inside the furnace, i.e.  $i = 1, \dots, 2N_v$  and  $j = 1, \dots, N_{slab}$ , can be assembled into a single system of ODEs with interconnections due to the radiative heat flows  $\dot{Q}_{g_i}$ ,  $\dot{Q}_{w_i}$ ,  $\dot{Q}_{s_j,u}$ , and  $\dot{Q}_{s_j,d}$  for  $i = 1, \dots, 2N_v$  and  $j = 1, \dots, N_{slab}$ . In view of the algebraic equations (24)-(28), this results in a differential algebraic description. However, the linear system of equations (25) and (26) for  $i = 1, \dots, 2N_v$  and  $j = 1, \dots, N_{slab}$  can be solved explicitly for the surface radiosities and irradiances  $J_{w_i} A_{w_i}$ ,  $J_{s_j}^i A_{s_j}^i$ ,  $\mathcal{E}_{w_i} A_{w_i}$ , and  $\mathcal{E}_{s_j}^i A_{s_j}^i$ . By using (24) and (28) this allows to explicitly determine the heat flows in terms of the gas compositions  $w_{g_i}^\nu$ , the gas temperatures  $T_{g_i}$ , the wall temperatures  $T_{w_i}$  and the slab temperatures  $T_{s_j,1}$  and  $T_{s_j,N_{s_j}}$  with  $i = 1, \dots, 2N_v$  and  $j = 1, \dots, N_{slab}$ . As a result, the system of differential algebraic equations (DAEs) is obviously of index one, which finally yields the furnace dynamics as a system of nonlinear ODEs

$$\frac{d}{dt} \begin{bmatrix} \mathbf{w}_g \\ \mathbf{T}_g \\ \mathbf{T}_w \\ \mathbf{T}_s \end{bmatrix} = \begin{bmatrix} \underline{f}_{w_g}(\mathbf{w}_g, \mathbf{T}_g, \mathbf{u}_g) \\ \underline{f}_{T_g}(t, \mathbf{w}_g, \mathbf{T}_g, \mathbf{T}_w, \mathbf{T}_s, \mathbf{u}_g) \\ \underline{f}_{T_w}(t, \mathbf{w}_g, \mathbf{T}_g, \mathbf{T}_w, \mathbf{T}_s) \\ \underline{f}_{T_s}(t, \mathbf{w}_g, \mathbf{T}_g, \mathbf{T}_w, \mathbf{T}_s) \end{bmatrix}, \quad (29)$$

<sup>1</sup>For a more detailed evaluation a CFD analysis could be performed. Nevertheless, for the purposes considered in this paper such a level of detail is not necessary.

with the vector  $\underline{w}_g = \{w_{g_i}\}_{i=1,\dots,2N_v}$  and the vector  $\mathbf{T}_g = \{T_{g_i}\}_{i=1,\dots,2N_v}$  composed of the mass fraction vectors of all control volumes and the gas temperatures inside all volumes, respectively. The vector  $\mathbf{T}_w = \{T_{w_i}\}_{i=1,\dots,2N_v}$  combines the temperatures of all walls and  $\underline{\mathbf{T}}_s = \{\mathbf{T}_{s_j}\}_{j=1,\dots,N_{\text{slab}}}$  is composed of all slab temperature vectors. Similarly to the state variables on the left hand side of (29), the functions on the right hand side are composed of the respective right hand sides of the sub-model ODEs. In detail, the vector  $\underline{\mathbf{f}}_{w_g} = \{\mathbf{f}_{w_{g_i}}\}_{i=1,\dots,2N_v}$  and the vector  $\mathbf{f}_{T_g} = \{f_{T_{g_i}}\}_{i=1,\dots,2N_v}$  are given by the right hand sides of (14) for all control volumes and the vector  $\mathbf{f}_{T_w}$  is composed of the right hand side of (16) for all walls. Finally, the vector  $\underline{\mathbf{f}}_{T_s} = \{\mathbf{f}_{s_j}\}_{j=1,\dots,N_{\text{slab}}}$  consists of the right hand side of (21) for all slabs inside the furnace. The input variables of the ODEs (29) follow as  $\underline{u}_g = \{u_{g_i}\}_{i=1,\dots,2N_v}$ , which combines the input variables of all individual control volumes. In summary, (29) represents the dominating dynamics of the considered pusher-type reheating furnace. Furthermore, recall that the pusher-type reheating furnace can be classified as a hybrid system due to the event driven slab movements as well as the charging and discharging process which is expressed in (29) by the explicit dependence on the time  $t$  of the functions on the right hand side. In addition, whenever slabs are charged or discharged the dimensions of  $\underline{\mathbf{T}}_s$  and  $\underline{\mathbf{f}}_{T_s}$  in (29) have to be adapted such that the dimension of the overall system (29) given as  $2N_v(\dim(G_e \cup G_a) + 2) + \sum_{j=1}^{N_{\text{slab}}} N_{s_j}$  in a typical operation mode varies approximately between 270 and 360.

For the numerical solution the set of ODEs (29) is implemented in MATLAB/SIMULINK. Therefore, the sub-models presented in Section 2 are implemented using the programming language C++. This allows to examine several furnace configurations with only small changes of the source code. In addition, this ensures simple portability of the implementation to the automation system of the plant. During the numerical solution the differential equations (29) are successively re-assembled and re-adapted according to the current charging situation inside the furnace. This includes the recurrent change of the model dimension.

## 5. Experimental model validation

In order to validate the developed mathematical model (29) a measurement campaign was performed at the AG der Dillinger Hüttenwerke in Dillingen, Germany. Therefore, a test slab equipped with thermocouples was reheated in the pusher-type reheating furnace schematically illustrated in Figure 1. Besides the already mentioned temperature measurement of the test slab, the wall surface temperatures and the exhaust gas compositions inside the funnel are additionally measured. Furthermore, the input variables  $\underline{u}_g$ , i.e. the mass flows of fuel and combustion air as well as their temperature are measured and are used as inputs for the numerical solution of (29) with a furnace discretization of  $N_v = 10$ . Note that subsequently all quantities are depicted in a normalized fashion with the time variable scaled by the duration of the measurement campaign  $t_E$ .

At first, a comparison of the simulated and measured exhaust gas composition is illustrated in Figure 7 where the normalized time-evolutions of the concentrations of  $\text{CO}_2$  and  $\text{O}_2$  inside the funnel are shown, respectively. Note that the depicted volumetric exhaust gas composition  $\bar{c}^\nu$ ,  $\nu \in \{\text{CO}_2, \text{O}_2\}$  inside the funnel can be easily obtained by considering the mixture of the mass flows  $\dot{m}_{g_1}^{\text{out}}$  and  $\dot{m}_{g_{N_v+1}}^{\text{out}}$ , i.e.

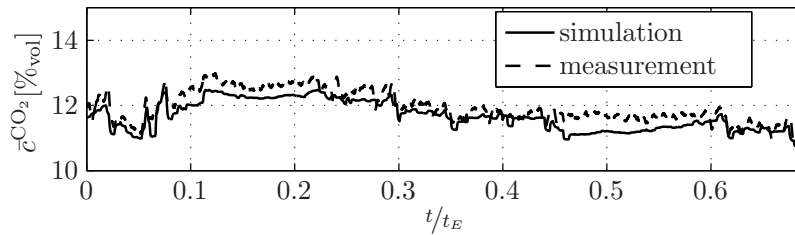
$$\bar{c}^{\text{CO}_2} = \frac{w_f^{\text{CO}_2}}{M_{\text{CO}_2} \sum_{\nu \in G_a \cup G_e} \frac{w_f^\nu}{M_\nu}}, \quad \bar{c}^{\text{O}_2} = \frac{w_f^{\text{O}_2}}{M_{\text{O}_2} \sum_{\nu \in G_a \cup G_e} \frac{w_f^\nu}{M_\nu}} \quad (30)$$

with the mass fractions of the exhaust gas flow in the funnel

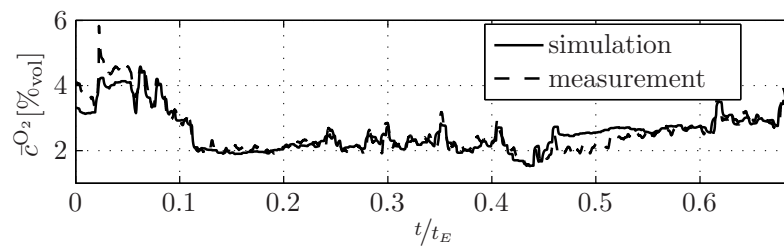
$$w_f^\nu = \frac{\dot{m}_{g_1}^{\text{out}} w_{g_1}^\nu + \dot{m}_{g_{N_v+1}}^{\text{out}} w_{g_{N_v+1}}^\nu}{\dot{m}_{g_1}^{\text{out}} + \dot{m}_{g_{N_v+1}}^{\text{out}}}, \quad \nu \in G_a \cup G_e.$$

Unfortunately, due to an unrecoverable failure of the corresponding measurement devices during the experiment, the time axis in Figure 7 is truncated at  $t/t_E \approx 0.7$ . Nevertheless, the superior agreement of

measured and simulated data confirms the accuracy and applicability of the presented modelling approach for the exhaust gas composition.



(a) Volumetric content of CO<sub>2</sub>.



(b) Volumetric content of O<sub>2</sub>.

Figure 7. Comparison of simulated and measured volumetric exhaust gas content in the funnel.

The normalized time-evolutions of the wall temperatures (normalized to the target temperature  $T_E$  of the test slab) are depicted in Figure 8, where the simulated and measured surface temperatures are compared at different locations on the upper and lower section of the furnace. Thereby, the measurement data are obtained from thermocouples located at the interior wall elements of the furnace. In particular, the wall temperatures are shown in representative control volumes of the pre-heating zone (Figure 8(a)), the heating zone (Figures 8(b), 8(c)), and the pre-soaking zone (Figure 8(d)). Obviously, the dynamics of the surface wall temperature including the heat exchange due to radiation is highly accurately reflected with only minor deviations between the simulated and measured results. It should be also pointed out that the small ripples, which are visible mainly in the results for the pre-heating and heating zone, occur due to the event-driven movement of the slabs. As is shown, these ripples are closely recovered in the determined simulation model.

In view of a possible application of the derived model to model-based control design and furnace optimization, it is required that the numerical solution accurately reproduces the actual slab temperature distribution. This is illustrated in Figure 9, where the simulated and measured slab temperatures (normalized to the target temperature  $T_E$  of the test slab) are compared at different locations over the height of the test slab. The considered locations are thereby fixed by technical reasons, which limit the possibilities to install thermocouples inside the test slab. As can be clearly deduced from Figure 9, an almost perfect match between the temperature evolutions close to the upper surface of the test slab (a), its core (b), and close to its lower surface (c) is obtained throughout the reheating process.

Together with the highly accurate reproduction of the exhaust gas composition and the wall temperatures, the comparison of the simulated and measured slab temperature distribution obviously confirms the applicability of the derived model to represent the dynamics of the considered pusher-type reheating furnace.

## 6. Conclusions

In this contribution a mathematical model of manageable complexity in view of the application of model-based control and optimization algorithms is determined for a commonly used pusher-type reheating

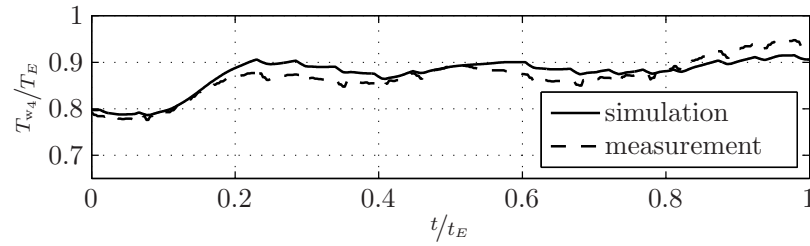
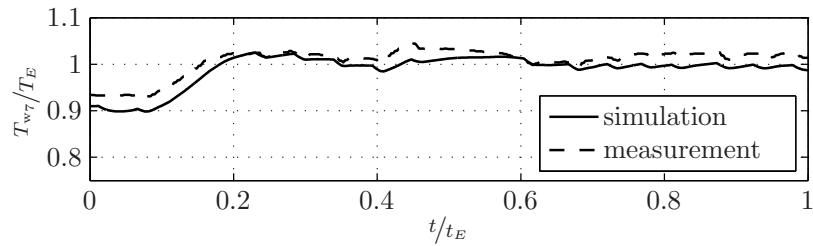
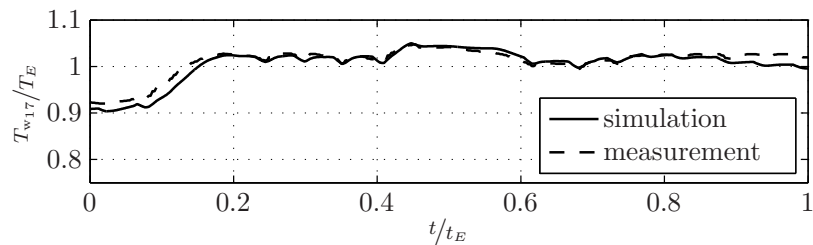
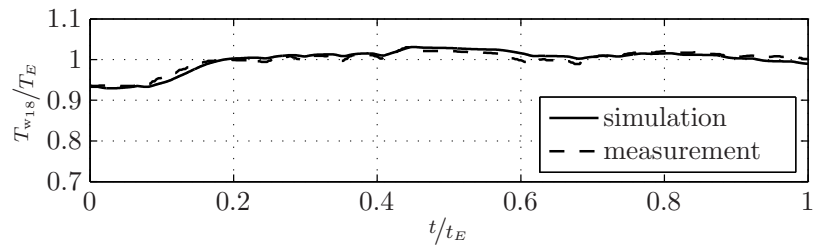
(a) Temperature  $T_{w_4}$  of a wall element located in the pre-heating zone of the upper furnace section.(b) Temperature  $T_{w_7}$  of a wall element located in the heating zone of the upper furnace section.(c) Temperature  $T_{w_{17}}$  of a wall element located in the heating zone of the lower furnace section.(d) Temperature  $T_{w_{18}}$  of a wall element located in the pre-soaking zone of the lower furnace section.

Figure 8. Comparison of simulated and measured wall surface temperatures for a representative variety of discretized wall elements in the pre-heating zone (a), the heating zone (b), (c), and the pre-soaking zone (d). The temperatures are normalized to the target temperature of the test slab  $T_E$ .

furnace. Similar to the zone method the furnace is decomposed into suitable control volumes whose upper and lower boundaries are given by the respective furnace walls and the slabs moving through the furnace. Besides the gas dynamics due to combustion and convection, the heat exchange due to radiation between the gaseous phase, the surrounding walls, and the slabs inside the furnace represents the dominating dynamics of the reheating process.

For modelling purposes, at first mass and energy balances are set up for each control volume in order to capture the combustion process. The complexity of the system description is reduced by applying the singular perturbation theory to eliminate the rather fast dynamics of the combustion process. The dynamics of the surface temperature of the furnace walls is approximated by an ODE taking into account the dynamics of a thin inner wall layer and the heat conduction through the outer wall layers. Due to the

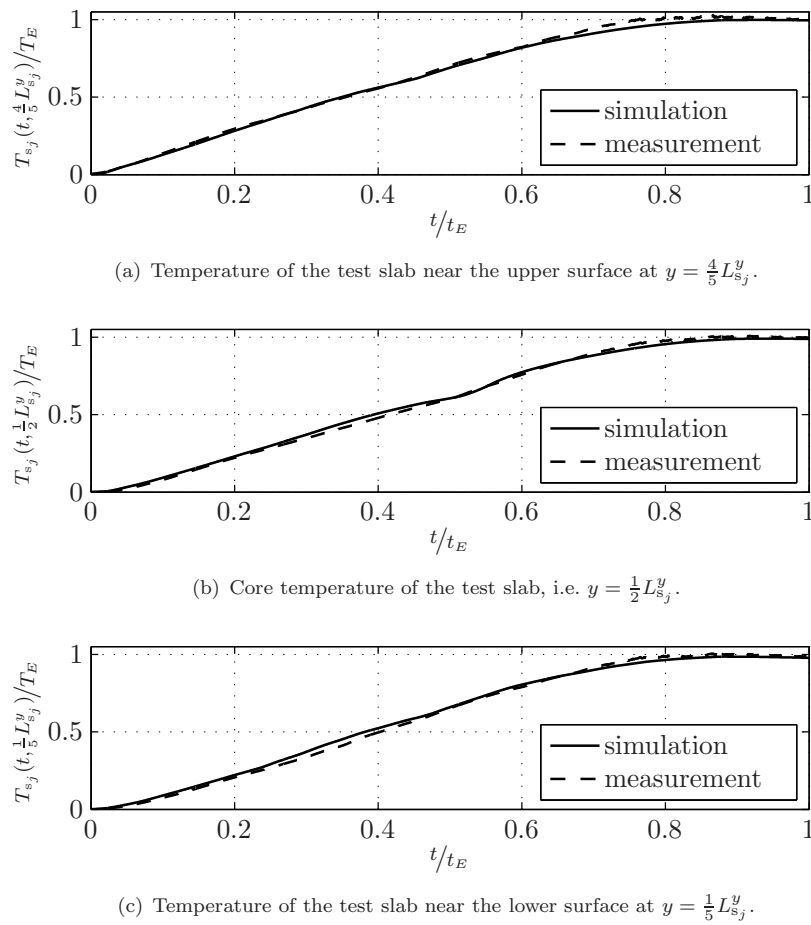


Figure 9. Comparison of simulated and measured normalized temperature distribution of the test slab at certain positions along the slab height.

broad temperature range the temperature distribution in each slab has to be described in terms of the heat equation with temperature-dependent parameters which is discretized by means of the finite difference method.

Since the sub-models obtained for each control volume are interconnected by the heat exchange due to radiation, the overall system model is determined in an assembly process by applying the so-called net radiation method. For the numerical simulation the resulting system of ODEs is implemented in MATLAB/SIMULINK. Due to the event-driven movement of the slabs, i.e. new slabs can only enter the furnace whenever reheated slabs are pushed out of the furnace, the system can be classified as a hybrid system. This significantly complicates the implementation because the sub-models have to be re-assembled whenever slabs enter or leave the furnace due to the changing radiative coupling of the slabs with their environment. In addition, the number of slabs inside the furnace varies, which results in a varying dimension of the system model.

Besides numerical analysis, the determined model of the reheating process is validated by experimental results obtained from a measurement campaign with a test slab equipped with thermocouples at the AG der Dillinger Hüttenwerke, Dillingen, Germany. The high accuracy of the model is thereby confirmed by comparing the time-evolutions of the simulated and measured exhaust gas composition, the wall temperatures as well as the slab temperatures. This in particular emphasizes the applicability of the considered approach in view of model-based control and optimization of the furnace operation.

## 7. Acknowledgments

The authors would like to thank the AG der Dillinger Hüttenwerke for the financial support, the fruitful discussions and in particular for supporting us in successfully accomplishing the measurement campaigns.

## References

- [1] Kim, M., 2007, A heat transfer model for the analysis of transient heating of the slab in a direct-fired walking beam type reheating furnace. *Int. Journal of Heat and Mass Transfer*, **50**, 2740–2748.
- [2] Kim, J.G. and Huh, K., 2000, Three-dimensional analysis of the walking-beam-type slab reheating furnace in hot strip mills. *Numerical Heat Transfer*, **48**, 589–609.
- [3] Boineau, P., Copin, C. and Aguilé, F., 2002, Heat transfer modelling using advanced zone model based on a CFD code. In: *Proceedings of the Proceedings of the 6th European Conference on Industrial Furnaces and Boilers (INFUB)*, Lisbon, Portugal, pp. 85–94.
- [4] Hackl, F., 1974, Eine betriebsorientierte Methode zur Berechnung der instationären thermischen Vorgänge in Wärmöfen. PhD thesis, Montanuniversität Leoben.
- [5] Jaklic, A., Vode, F. and Kolenko, T., 2007, Online simulation model of the slab-reheating process in a pusher-type furnace. *Applied Thermal Engineering*, **5-6**, 1105–1114.
- [6] Marino, P.A., Pignotti, A. and Solis, D., 2002, Numerical model of steel slab reheating in pusher furnaces. *Latin American Applied Research*, **32**(3), 257–261.
- [7] Cohen, E.S., 1951, Effect of gas temperature gradients on radiant heat transmission. PhD thesis, Massachusetts Institute of Technology.
- [8] Korndorfer, U., 1975, Mathematisches Modell zur Beschreibung der Wärmeübertragung in Stoßöfen. PhD thesis, Universität Karlsruhe.
- [9] Stracke, H., 1979, Der Einfluß der Gasstrahlung auf den Wärmeübertrag im Stoßofen - ein mathematisches Modell. PhD thesis, RWTH Aachen.
- [10] Rhine, J.M. and Tucker, R.J., 1991 *Modelling of gas-fired furnaces and boilers* (London, New York: British Gas, McGraw-Hill Book Company).
- [11] Turns, S.R., 2000 *An Introduction to Combustion*, 2 (Boston: McGraw-Hill).
- [12] Stephan, P., Schaber, K., Stephan, K. and Mayinger, F., 1999 *Thermodynamik 2, Mehrstoffsysteme*, 14 (Berlin: Springer-Verlag).
- [13] Khalil, H., 2002 *Nonlinear Systems*, 3 (New Jersey: Prentice Hall).
- [14] Baehr, H.D. and Stephan, K., 2006 *Heat and Mass Transfer*, 2 (Berlin, Heidelberg: Springer).
- [15] Woelk, G., 1966, Die Bestimmung der Temperatur in einer Ofenwand bei Berücksichtigung temperaturabhängiger Wärmeleitfähigkeit. *Gaswärme*, **15**(5), 138–142.
- [16] Laturell, E., 1968, Untersuchung der Kühlwirkung von Stoßofen-Gleitschienen mit Hilfe eines thermoelektrischen Analogiemodells. PhD thesis, Technische Universität Clausthal.
- [17] Harste, K., 1989, Untersuchung zur Schrumpfung und zur Entstehung von mechanischen Spannungen während der Erstarrung und nachfolgender Abkühlung zylindrischer Blöcke aus Fe-C-Legierungen. PhD thesis, Technische Universität Clausthal.
- [18] Thomas, J.W., 1995 *Numerical Partial Differential Equations: Finite Difference Methods*, no. 22 In: *Texts in Applied Mathematics* (New York, Berlin, Heidelberg: Springer-Verlag).
- [19] Kofstad, P., 1988 *High temperature corrosion* (London and New York: Elsevier Applied Science).
- [20] Hottel, H.C. and Egbert, R.B., 1941, The Radiation of Furnace Gases. *Trans. of the A.S.M.E.*, **63**, 297–307.
- [21] Schack, K., 1970, Berechnung der Strahlung von Wasserdampf und Kohlendioxid. *Chemie Ingenieur Technik*, **42**(2), 53–58.
- [22] Hottel, H.C. and Sarofim, A.F., 1967 *Radiative Transfer* (New York: McGraw-Hill Book Company).
- [23] Walton, G.N., 2002, Calculation of Obstructed View Factors by Adaptive Integration. Technical report MD. NISTIR 6925, National Institute of Standards and Technology (NISTIR), Gaithersburg.